

**SYNTHESIS, CHARACTERIZATION AND  
THEORETICAL STUDIES ON A NEW  
DONOR-PI-ACCEPTOR (D- $\pi$ -A) BRIDGE  
SYSTEM OF FERROCENYL CHALCONES FOR  
POTENTIAL SOLAR CELL APPLICATIONS**

**AINIZATUL HUSNA BINTI ANIZAIM**

**UNIVERSITI SAINS MALAYSIA**

**2021**

**SYNTHESIS, CHARACTERIZATION AND  
THEORETICAL STUDIES ON A NEW  
DONOR-PI-ACCEPTOR (D- $\pi$ -A) BRIDGE  
SYSTEM OF FERROCENYL CHALCONES FOR  
POTENTIAL SOLAR CELL APPLICATIONS**

by

**AINIZATUL HUSNA BINTI ANIZAIM**

**Thesis submitted in fulfilment of the requirements  
for the degree of  
Master of Science**

**October 2021**

## ACKNOWLEDGEMENT

I would like to express my gratitude to Allah SWT for giving me strength and blessing throughout my journey to complete this master's thesis successfully. In this opportunity, I want to convey my gratitude to my main supervisor, Dr. Suhana Arshad, who had spent her valuable time guiding and helping me despite of her busy schedule. She had been very patience and enthusiastic when giving me encouragement and useful critiques for better improvement to my research till the end. My sincere thanks also go to my co-supervisor, Professor Dr. Abdul Razak Ibrahim for the aspiring guidance and insightful comments throughout my study.

My deepest thanks goes to my fellow labmate, Mr. Fikri Zaini who never hesitate to teach, help and give me his ideas regarding on my research project. Not to forget, my appreciation to Dr. Dian Alwani and Ms. Wong Qin Aii who had been very helpful in sharing their knowledge specifically during my early stage of research. Besides, I would like to give special thanks to all X-ray Crystallography laboratory staff especially Mr. Aswafi, Mr. Mustaqim Rosli and Mr. Mustaqim Abu Bakar for their support and assistance in conducting my research project. Also, thanks to my other labmates, Ms. Aliya, Ms. Farhana, Ms. Heng and Mr. Salleh for handing your hand whenever I am in needs.

I wish to acknowledge the support and love of my parents, Mr. Anizaim and Mrs. Fazilah. Thank you Mama and Ayah for your continuous prayers throughout my study. Specials thanks also to my sisters, Hafizah, Aimi Nabila and Anis Ameera for their continuous support especially in terms of financial during my study.

Apart from that, I feel so grateful to have a supportive partner, Dr. Aizat Shamsuddin who has always motivated me through the process of researching and writing this thesis. This journey is tough, he is the one who persuade me to never give up and always cherish my good moment.

I want to thank to the Malaysian government and the Universiti Sains Malaysia for their financial support for this work through the Fundamental Research Grant Scheme (No: 203.PFIZIK.6711606) and the Research University Grant (No: 1001.PFIZIK.8011115). My grateful thanks are also extended to MARA for supporting my tuition fee during my study.

Last but not least, a huge thank you to everyone not mentioned here that has been a part of my life directly or indirectly during my master's journey. Thank you so much! The moment I write here, we are all still struggling with MCO 3.0. I wish everyone is continued a good health and stay safe.

## TABLE OF CONTENTS

<b>ACKNOWLEDGEMENT</b> .....	<b>ii</b>
<b>TABLE OF CONTENTS</b> .....	<b>iv</b>
<b>LIST OF TABLES</b> .....	<b>viii</b>
<b>LIST OF FIGURES</b> .....	<b>ix</b>
<b>LIST OF ABBREVIATIONS</b> .....	<b>xiv</b>
<b>LIST OF APPENDICES</b> .....	<b>xvii</b>
<b>ABSTRAK</b> .....	<b>xviii</b>
<b>ABSTRACT</b> .....	<b>xix</b>
<b>CHAPTER 1 INTRODUCTION</b> .....	<b>1</b>
1.1 Chalcone and Ferrocenyl Chalcone derivatives .....	1
1.2 The push-pull configuration of the $\pi$ -conjugated bridge system .....	3
1.3 The generation of solar cell application and materials .....	4
1.4 Problem Statement .....	6
1.5 Objectives .....	7
<b>CHAPTER 2 LITERATURE REVIEW</b> .....	<b>8</b>
2.1 Synthesis of Ferrocenyl Chalcone Derivatives .....	8
2.2 Fourier Transform Infrared (FTIR) Vibrational Studies .....	11
2.3 Nuclear Magnetic Resonance (NMR) Studies .....	14
2.4 UV-Visible Spectroscopic Studies .....	16
2.5 X-ray Diffraction Studies .....	22
2.5.1 <i>Cis, trans, s-cis</i> and <i>s-trans</i> configurations .....	22
2.5.2 Crystal packing .....	24
2.6 Density Functional Theory (DFT) .....	26
2.6.1 HOMO-LUMO analysis .....	26
2.6.2 Molecular Electrostatic Potential .....	29

2.7	Solar Cell Application .....	31
<b>CHAPTER 3 THEORY AND METHODOLOGY.....</b>		<b>34</b>
3.1	The Synthesis of Ferrocenyl Chalcone Derivatives .....	37
3.2	Fourier Transform Infrared Spectroscopy (FTIR) Analysis.....	38
3.2.1	General Theory of FTIR .....	38
3.2.2	Sample Preparation and Instrumentation .....	40
3.3	Nuclear Magnetic Resonance (NMR) Studies .....	41
3.3.1	General Theory of NMR .....	41
3.3.2	Sample Preparation for NMR .....	42
3.3.3	Instrumentation for NMR analysis .....	43
3.4	Ultraviolet-Visible (UV-Vis) Studies .....	44
3.4.1	General Theory of UV-Vis .....	44
3.4.2	Preparation of Samples .....	44
3.4.3	Instrumentation and software .....	45
3.5	X-ray Studies .....	46
3.5.1	General Theory of X-ray .....	46
3.5.2	X-ray Crystallographic Procedure .....	47
3.5.3	X-Ray Single Crystal Instrumentation .....	49
3.6	Density Functional Theory (DFT) Studies .....	50
3.7	Solar Cell Applications .....	50
3.7.1	Preparation of DSSC .....	52
3.7.2	Characterization and performance study of DSSC .....	53
3.7.3	Instrumentation of solar cell study .....	55
<b>CHAPTER 4 RESULTS AND DISCUSSION .....</b>		<b>61</b>
4.1	Fourier Transform Infrared (FTIR) Spectroscopic Analysis .....	56
4.2	Nuclear Magnetic Resonance (NMR) Spectroscopic Analysis .....	60
4.3	Molecular, Crystal and Optimized Structure Analyses .....	63

4.4	Energy Gap Studies .....	81
4.4.1	UV-Vis Analysis .....	81
4.4.2	HOMO-LUMO Analysis.....	92
4.5	Molecular Electrostatic Potential (MEP) .....	92
4.6	Solar Cell Application .....	97
4.6.1	FESEM and Energy Dispersive X-ray (EDX) Analyses .....	102
4.6.2	Solar Cell Performance Study .....	105
<b>CHAPTER 5 CONCLUSION AND FUTURE RECOMMENDATIONS ....</b>		<b>111</b>
5.1	Conclusion .....	106
5.2	Future Recommendations .....	108
<b>REFERENCES .....</b>		<b>114</b>
<b>APPENDICES</b>		
<b>LIST OF PUBLICATIONS</b>		

## LIST OF TABLES

	<b>Page</b>
Table 2.1	List of the reported single crystals of ferrocenyl chalcones from previous studies.....9
Table 2.2	Assignment of some characteristic vibrational frequencies of ferrocenyl chalcone .....12
Table 2.3	<sup>1</sup> H isotropic chemical shifts (ppm).....14
Table 2.4	<sup>13</sup> C isotropic chemical shifts (ppm) .....15
Table 2.5	The $\lambda_{\text{max}}$ (in nm) and energy band gap (in eV) of ferrocenyl chalcones from previous studies .....17
Table 2.6	UV-Vis absorption maximum of the compound in different solvents (Trujillo <i>et al.</i> , 2017).....19
Table 2.7	Some characterization of different R-groups substituents in ferrocenyl chalcone .....21
Table 2.8	The summary of power conversion efficiency of <b>(a)</b> , <b>(b)</b> and <b>(c)</b> (Chauhan <i>et al.</i> , 2016).....32
Table 2.9	Summary of DSSCs performance for compounds (Phan <i>et al.</i> , 2019) .....34
Table 2.10	The summary of power conversion efficiency of a and b (Teo <i>et al.</i> , 2017) .....35
Table 4.1	The vibrational results of ferrocenyl chalcones <b>(1-15)</b> .....57
Table 4.2	The <sup>1</sup> H NMR isotropic chemical shifts (ppm) .....60
Table 4.3	The <sup>13</sup> C NMR isotropic chemical shifts (ppm) .....61
Table 4.4	Crystal data and structure refinement .....64
Table 4.5	The selected experimental bond length, bond angle and torsion angle of <b>1-5</b> .....66



Table 4.6	The dihedral angles formed between enone moiety and aromatic rings.....	68
Table 4.7	Hydrogen bond geometry of <b>1-5</b> .....	71
Table 4.8	The selected theoretical bond length, bond angle and torsion angle of all ferrocenyl chalcone .....	79
Table 4.9	Experimental and calculated substituent effects on the $\lambda_{\text{max}}$ (nm) of ferrocenyl chalcones .....	83
Table 4.10	MEP plot of ferrocenyl chalcones.....	92
Table 4.11	The element weight percentage for all compounds.....	98
Table 4.12	Solar cell parameters and performance of ferrocenyl chalcones .....	103

## LIST OF FIGURES

	<b>Page</b>
Figure 1.1	The general schematic diagram of chalcone derivative (Romanelli <i>et al.</i> , 2011) ..... 1
Figure 1.2	The eclipsed and staggered configurations of ferrocene (Astruc, 2017) ..... 2
Figure 1.3	General structure of Type 1 and Type 2 of ferrocenyl chalcone (Henry <i>et al.</i> , 2020) ..... 3
Figure 1.4	(a) The push-pull configuration of chalcone derivative (Zhuang <i>et al.</i> , 2018); (b) the D- $\pi$ -A bridge system of chalcone (Shkir <i>et al.</i> , 2017) ..... 3
Figure 1.5	The first, second and third generation of solar cells (Organic Photovoltaics, n.d)..... 5
Figure 1.6	The structure of DSSC (Ali <i>et al.</i> , 2016) ..... 5
Figure 2.1	Synthesis scheme of (2 <i>E</i> )-1-ferrocenyl-3-phenyl-prop-2-en-1-one (Yadav <i>et al.</i> , 2019)..... 8
Figure 2.2	Synthesis scheme of ferrocenyl chalcone (Chauhan <i>et al.</i> , 2016)..... 9
Figure 2.3	FTIR spectrum of methyl pyrimidine substituted ferrocenyl chalcone (Twinkle <i>et al.</i> , 2020)..... 13
Figure 2.4	The assignment of <sup>1</sup> H NMR of ferrocenyl chalcone ..... 14
Figure 2.5	The spectrum of (a) <sup>1</sup> H NMR and (b) <sup>13</sup> C NMR (Yadav <i>et al.</i> , 2019) ..... 16
Figure 2.6	Absorption spectrum of ( <i>E</i> )-chalcone (Jumina <i>et al.</i> , 2019)..... 17
Figure 2.7	Absorption spectra of compounds (Maynadié <i>et al.</i> , 2006)..... 18
Figure 2.8	The experimental absorption spectra of $1.1 \times 10^{-4}$ mM ( <i>E</i> )-3-Ferrocenyl-1-(2-hydroxy-4-methoxyphenyl)-prop-2-en-1-one in different solvents (Trujillo <i>et al.</i> , 2017) ..... 20

Figure 2.9	UV-Vis spectra of 7 ferrocenyl chalcones in acetonitrile (Muller <i>et al.</i> , 2012) .....	21
Figure 2.10	Different type of configurations in chalcone .....	22
Figure 2.11	Molecular structures of (a) Fc-Anth and (b) Anth-Fc (Jung <i>et al.</i> , 2008) .....	23
Figure 2.12	Molecular structure of (a) (2 <i>E</i> )-1-(2,4-difluorophenyl)-3-ferrocenyl-2-propen-1-one and (b) (2 <i>E</i> )-1-(2-furanyl)-3-ferrocenyl-2-propen-1-one (Attar <i>et al.</i> , 2011) .....	23
Figure 2.13	(a) The ORTEP diagram; (b) The crystal packing of ( <i>E</i> )-3-(4-bromophenyl)-1-(3,4-dimethoxyphenyl)prop-2-en-1-one (Kwong <i>et al.</i> , 2018) .....	24
Figure 2.14	(a) The ORTEP diagram; (b) The crystal packing of 1-(4-methoxyphenyl)-3-(4- <i>N,N</i> -dimethyl amino phenyl)-2-propen-1-one (Zhao <i>et al.</i> , 2021) .....	25
Figure 2.15	The packing of the chalcone derivative (Anizaim <i>et al.</i> , 2019) .....	25
Figure 2.16	The HOMO-LUMO distributions of ferrocenyl chalcones (Khan <i>et al.</i> , 2017) .....	27
Figure 2.17	The charge density distribution of the HOMO-LUMO for Q1 and Q2 dyes (Al-Horaibi <i>et al.</i> , 2018) .....	27
Figure 2.18	Schematic view for time scales of charge transport in a typical DSSC (Fallah <i>et al.</i> , 2020) .....	28
Figure 2.19	Molecular electrostatic potential surface of (a) (2 <i>E</i> )-1-(5-bromothiophen-2-yl)-3-(3-fluorophenyl) prop-2-en-1-one and (b) (2 <i>E</i> )-1-(5-bromothiophen-2-yl)-3-(4-methoxyphenyl) prop-2-en-1-one (Naik <i>et al.</i> , 2020) .....	29
Figure 2.20	Molecular electrostatic potential (MEP) maps of pyrazolic compounds (Tighadouini <i>et al.</i> , 2020) .....	30
Figure 2.21	The ORTEP diagram of <b>a</b> , <b>b</b> and <b>c</b> and J-V curves of DSSCs for the compounds (Chauhan <i>et al.</i> , 2016) .....	32

Figure 2.22	(a) The compounds with different electron donors and acceptor; (b) <i>J/V</i> measurement of the compounds (Phan <i>et al.</i> , 2019).....	33
Figure 2.23	The <i>J/V</i> measurement of compound <b>a</b> and <b>b</b> (Teo <i>et al.</i> , 2017).....	35
Figure 3.1	The outline of research flow in this study .....	36
Figure 3.2	Synthesis of Ferrocenyl Chalcones ( <b>1-15</b> ) .....	37
Figure 3.3	Example of functional groups absorption in IR spectrum (Nandiyanto <i>et al.</i> , 2019) .....	39
Figure 3.4	Vibration modes of stretching and bending (Cameron <i>et al.</i> , 2020) .....	39
Figure 3.5	(a) PerkinElmer System 2000 FTIR Spectrometer; (b) PerkinElmer Spectrum .....	40
Figure 3.6	Simplified correlation chart for proton and carbon chemical shift values (Carey, 2018) .....	41
Figure 3.7	The example of multiple peaks for <sup>1</sup> H NMR (Ouellette & Rawn, 2018) .....	42
Figure 3.8	Thin NMR tube .....	43
Figure 3.9	(a) Bruker 500 and 125 MHz Avance III spectrometer; (b) Bruker TOPSPIN 2.1 software package.....	43
Figure 3.10	Electronic energy levels and transition (Akash & Rehman, 2019)....	44
Figure 3.11	(a) Bruker 500 and 125 MHz Avance III spectrometer; (b) Bruker TOPSPIN 2.1 software package.....	45
Figure 3.12	(a) UV-Visible Spectrophotometer Model Cary 5000 UV-Vis- NIR; (b) Origin8.5 software .....	45
Figure 3.13	(a) Diffraction according to Bragg's law (Pevelen, 2010); (b) Diffraction spots (Campana & Corporation, 2015); (c) Contour map of the electron density (Spek, 2018); (d) Molecular structure (Spek, 2018). .....	47
Figure 3.14	Mounted compound <b>1</b> on the fibre tip.....	47
Figure 3.15	The diffraction spots of compound <b>1</b> .....	48

Figure 3.16	Bruker APEX II Duo CCD diffractometer.....	49
Figure 3.17	(a) Schematic diagram of the DSSC structure layered; (b) Operation principles of a typical DSSC .....	51
Figure 3.18	The process of staining the working electrode and putting two electrodes together .....	53
Figure 3.19	(a) FEI Nova NanoSEM 450 scanning electron microscope for FESEM; (b) Computer used for EDX analysis; (c) Solar simulator ..	55
Figure 4.1	The assignment of proton and carbon NMR in ferrocenyl chalcone .....	60
Figure 4.2	The molecular structure of compound <b>1-5</b> with 30% ellipsoid.....	67
Figure 4.3	The dihedral angle between substituted Cp ring and substituent aromatic ring for compound <b>1-5</b> .....	70
Figure 4.4	A view that showing weak C–H···F interactions as in cyan dashed lines along the a-axis of the crystal packing of <b>1</b> .....	72
Figure 4.5	Packing diagram showing (a) a centrosymmetric dimer by weak intermolecular C19–H19A···F1 and C4–H4A···F1 interactions shown as blue dotted lines; (b) A partial parts of C20–H20C···O1 interactions; (c) The head-to-tail arrangement of C20–H20A···Cg1 of compound <b>2</b> .....	74
Figure 4.6	Packing diagram showing C–H···O and C–H··· $\pi$ interactions of compound <b>3</b> .....	75
Figure 4.7	The 2D packing showing weak C–H···O interactions (cyan dotted lines) of compound <b>4</b> .....	76
Figure 4.8	The 2D packing showing weak C–H···O (cyan dotted lines) and $\pi$ ··· $\pi$ (magenta dotted lines) interactions of compound <b>5</b> .....	77
Figure 4.9	The optimized structure of <b>1-15</b> utilizing B3LYP/6-311++G(d,p) basis set .....	78
Figure 4.10	Ring A and Ring B of the ferrocenyl chalcone .....	81
Figure 4.11	HOMO and LUMO energy levels of all compounds.....	89

Figure 4.12 FESSEM images of ferrocenyl chalcones (**1-15**) with magnifications of x10 000.....97

## LIST OF ABBREVIATIONS

A	Acceptor
ATR	Attenuated Total Reflectance
B3LYP	Becke's nonlocal three parameter exchange and the Lee, Young and Parr
CCD	Charge-Coupled Device
CCDC	The Cambridge Crystallographic Data Centre
CDCl <sub>3</sub>	Deuteriochloroform
CIF	Crystallographic Information File
CSD	Cambridge Structural Database
D	Donor
DFT	Density Functional Theory
DMSO	Dimethyl Sulfoxide
DSSC	Dye-sensitized Solar Cell
EtOH	Ethanol
FTIR	Fourier Transform Infrared
HOMO	Highest Occupied molecular Orbital
ICT	Intramolecular Charge Transfer
LUMO	Lowest Unoccupied Molecular Orbital
MEP	Molecular Electrostatic Potential
NaOH	Sodium Hydroxide
NMR	Nuclear Magnetic Resonance
NOR Lab	Nano-Optoelectronics Research & Technology Laboratory
ORTEP	Oak Ridge Thermal Ellipsoid Plot

ppm	Parts per million
SADABS	Siemens Area Detector Absorption Correction
SAINT	SAX Area-detector Integration (SAX-Siemens Analytical X-ray)
SMART	Siemens Molecular Analysis Research Tools
TD-DFT	Time Dependent Density Functional Theory
TMS	Tetramethylsilane
USM	Universiti Sains Malaysia
UV	Ultraviolet
UV-Vis	Ultraviolet Visible



## LIST OF APPENDICES

Appendix A	List of aldehydes of all compounds.
Appendix B	FTIR spectra of all compounds.
Appendix C	$^1\text{H}$ and $^{13}\text{C}$ NMR spectra of all compounds.
Appendix D	Theoretical UV-Vis spectra of all compounds.
Appendix E	Solar cell performance of all compounds.

**SINTESIS, PENCIRIAN DAN KAJIAN TEORI KE ATAS SISTEM  
JAMBATAN PENDERMA- $\pi$ -PENERIMA (D- $\pi$ -A) KALKON FEROSENIL  
BAHARU UNTUK POTENSI APLIKASI SEL SURIA**

**ABSTRAK**

15 sebatian organometalik yang dikenali sebagai kalkon ferosenil telah direka untuk digunakan di dalam aplikasi sel suria peka pewarna (DSSC) berdasarkan pada binaan penderma- $\pi$ -penerima (D- $\pi$ -A). Sebatian-sebatian tersebut secara strategiknya telah berjaya disintesis dengan mengenakan penggantian yang berbeza melalui kaedah pemewapan Claisen-Schmidt dan telah menghasilkan 5 kristal tunggal kalkon ferosenil. Kesemua sebatian yang telah disintesis kemudiannya dicirikan dengan menggunakan kaedah IR dan NMR. Kajian spektroskopi UV-Vis telah menunjukkan pergeseran batokromik sehingga 500 nm dalam spektrum untuk kesemua kalkon ferosenil yang mana nilai tersebut adalah sesuai untuk aplikasi DSSCs. Sebatian sasaran telah dikaji dengan lebih lanjut menggunakan analisis sinar-X dan dikaji dengan menggunakan kaedah pengkomputeran Teori Fungsi Ketumpatan (DFT) untuk menyelidik potensi kalkon ferosenil dalam DSSC. Gantian yang berbeza di dalam lima hablur tunggal kalkon ferosenil telah terbukti dapat menambah baik pemindahan caj intramolekul (ICT) dengan meningkatkan kelarasan tulang belakang satah sebatian. Padatan hablur menunjukkan susunan dari kepala ke ekor dan sisi ke sisi melalui interaksi antara molekul C-H $\cdots$ O, C-H $\cdots$ F, C-H $\cdots$  $\pi$  and  $\pi\cdots\pi$ . Potensi Elektrostatik Molekul (MEP) menunjukkan kekuatan sesuatu sistem tolak-tarik bagi kesemua sebatian yang digambarkan melalui kawasan elektrostatik positif, negatif dan neutral. Di samping itu, semua kalkon ferosenil menunjukkan tahap tenaga HOMO yang terletak di bawah potensi redoks elektrolit dan tahap tenaga LUMO yang berada di

atas jalur konduksi permukaan  $\text{TiO}_2$ , menandakan bahawa sabatian tersebut mempunyai kesesuaian dan kemampuan untuk digunakan sebagai bahan peka pewarna. Berdasarkan hasil analisis molekul dan fotofizikal, kecekapan penukaran kuasa bagi kebolehan peka pewarna dalam DSSC telah ditingkatkan oleh sebatian yang mempunyai konfigurasi yang lebih satah, interaksi antara molekul dalam susunan padatan hablur dari sisi ke sisi, penyerapan spektrum yang besar dalam julat yang kelihatan dan kesetaraan tahap tenaga HOMO-LUMO.

**SYNTHESIS, CHARACTERIZATION AND THEORETICAL STUDIES ON  
A NEW DONOR- $\pi$ -ACCEPTOR (D- $\pi$ -A) BRIDGE SYSTEM OF  
FERROCENYL CHALCONES FOR POTENTIAL SOLAR CELL  
APPLICATIONS**

**ABSTRACT**

15 organometallic compounds known as ferrocenyl chalcones were designed for application in dye-sensitized solar cell (DSSC) based on a donor- $\pi$ -acceptor (D- $\pi$ -A) architecture. The compounds were strategically synthesized using Claisen-Schmidt condensation method by introducing different substituents and successfully yielded 5 single crystals of ferrocenyl chalcones. All synthesized compounds were further characterized using IR and NMR methods. The UV-Vis spectroscopic study revealed the spectrum for all ferrocenyl chalcones are bathochromically shifted up to 500 nm which are suitable for DSSCs application. Target compounds were further investigated by X-ray analysis and studied computationally using Density Functional Theory (DFT) approach to explore the potential in DSSCs. Different substituents in five ferrocenyl chalcone single crystals have been proven in enhancing intramolecular charge transfer (ICT) by improving the planarity of the compounds' backbone. The crystal packings show the head-to-tail and side by side arrangements *via* intermolecular C-H $\cdots$ O, C-H $\cdots$ F, C-H $\cdots$  $\pi$  and  $\pi\cdots\pi$  interactions. The molecular electrostatic potential (MEP) illustrates the strength of the push-pull system by the positive, negative, and neutral electrostatic potential sites of all compounds. Furthermore, all HOMO-LUMO energy levels of ferrocenyl chalcones are lied below the redox potential of electrolyte and above the conduction band of TiO<sub>2</sub> surface, respectively, indicating the suitability of the compounds to be potentially used as

photosensitizer materials. Based on the results of molecular and photophysical analyses, the power conversion efficiencies were enhanced by compounds with more planar configuration, side-by-side arrangement of the molecules in the crystal packing, large absorption spectra within the visible range and equivalent HOMO-LUMO energy levels for reliable DSSC photosensitizers.

# CHAPTER 1

## INTRODUCTION

### 1.1 Chalcone and Ferrocenyl Chalcone derivatives

Chalcone derivative ( $\text{Ar}-\text{COCH}=\text{CH}-\text{Ar}'$ ) belongs to the aromatic ketones family, in which two aromatic groups are associated by a carbonyl group and two  $\alpha,\beta$ -unsaturated carbon atoms (Romanelli *et al.*, 2011) as shown in Figure 1.1.

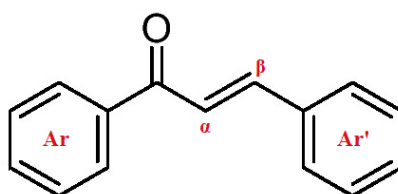


Figure 1.1 The general schematic diagram of chalcone derivative (Romanelli *et al.*, 2011).

Chalcones were discovered by Kostanecki and Tampar in 1899, are abundant in edible plants and also an intermediate precursor of flavonoids and isoflavonoids (Teo *et al.*, 2017). In recent times, chalcones can be synthesized by a Claisen-Schmidt condensation between benzaldehyde and acetophenone in the presence of sodium hydroxide (NaOH) as a catalyst. Chalcones have interesting characteristics such as large absorption coefficient in the UV range and good light-harvesting efficiency for solar application (Amogne *et al.*, 2020). Chalcone derivatives are commonly utilized in electrochemical sensing (Delavaux-Nicot *et al.*, 2007), optical limiting (Poornesh *et al.*, 2010), photo-initiated polymerization (Tehfe *et al.*, 2014) and non-linear optics (Teo *et al.*, 2017).

Ferrocene was discovered in 1951 and revolutionized the views of chemists on how metals bind to organic  $\pi$ -systems (Salzner, 2013). Ferrocene derivative has a unique sandwich structure in which the ferrous ion ( $\text{Fe}^{2+}$ ) is attached to the  $\pi$ -orbitals

of two cyclopentadienyl (Cp) rings (Paul *et al.*, 2019). According to Nemnes & Nicolaev (2014), ferrocene derivative may rotate about the Cp–Fe–Cp axis with two different configurations, which are eclipsed and staggered (Figure 1.2). In the ground state, these configurations are existed in condensed and gas phases, respectively.

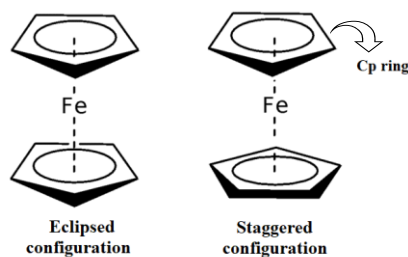


Figure 1.2 The eclipsed and staggered configurations of ferrocene (Astruc, 2017).

Ferrocene derivative has a broad absorption wavelength approximately 520 nm (Chauhan *et al.*, 2016), stable compound up to 400 °C (House, 2013) and has good redox property (Astruc, 2017). Based on this information, Ding and his co-workers (2015) have reported the used of ferrocene as part of material in battery, owing to rapid ferrocene/ferrocenium redox reaction. Ferrocene also gives a good solubility in most of the common organic solvents (Paul *et al.*, 2019).

Ferrocenyl chalcone is a structure consists of ferrocene moiety and aromatic unit terminal connected by the  $\alpha$ - $\beta$ -unsaturated carbonyl system (Figure 1.3). Ferrocenyl chalcones are classified into Type 1 and Type 2 depending on the position of the carbonyl group that attached to the ferrocene ring (Henry *et al.*, 2020). According to Trujillo *et al.* (2017), the synthesis of ferrocenyl chalcone derivatives by the Claisen-Schmidt condensation method is a green synthetic approach in ambient reaction with cheaper cost compared to the other conventional synthetic procedure which generate low yield, high amount of waste and unwanted by-product.

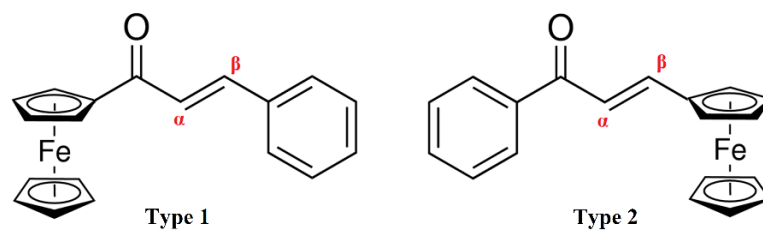


Figure 1.3 General structure of Type 1 and Type 2 of ferrocenyl chalcone (Henry *et al.*, 2020).

## 1.2 The push-pull configuration of the $\pi$ -conjugated bridge system

Chalcone derivatives as organic push-pull molecule (Figure 1.4a) are considered to have a strong donor-acceptor intermolecular interaction (Karaca *et al.*, 2018) and uplift the charge transfer within the molecules. Chalcone derivatives can easily be tuned into the desire compound by matching the suitable donor and acceptor substituent (Kumar *et al.*, 2012). Designing new materials with Donor(D)- $\pi$ -Acceptor(A) bridge system as shown in Figure 1.4b is important for enhancing the physical and chemical properties of the compound (Chavan *et al.*, 2016; Baggio *et al.*, 2016; Shkir *et al.*, 2017).

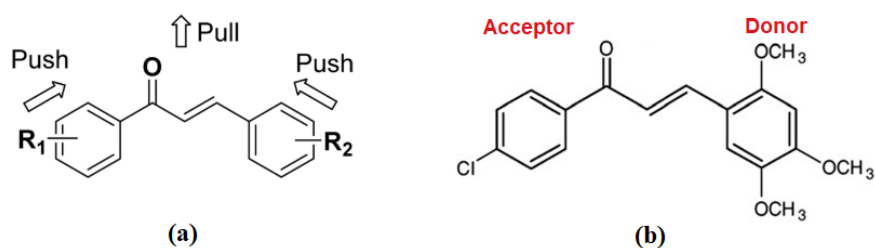


Figure 1.4 (a) The push-pull configuration of chalcone derivative (Zhuang *et al.*, 2018); (b) the D- $\pi$ -A bridge system of chalcone (Shkir *et al.*, 2017).

Ferrocenyl chalcone (Type 1) with D- $\pi$ -A bridge system is a bulky electron rich compound that exhibits a good electronic communication of intramolecular charge transfer (ICT) between the ferrocene donor and substituted acceptor (Chauhan *et al.*, 2016). The acceptor substituent can be varied from weak to strong electron-



withdrawing groups (EWG) such as -F, -Cl, -Br, -CN and -NO<sub>2</sub>. The D- $\pi$ -A configuration of ferrocenyl chalcone acts as push-pull architecture is believed to facilitate the movement of electron, increase photo stability and prevent dye aggregation in DSSC application (Shalini *et al.*, 2016; Lee *et al.*, 2017). Furthermore, the influence D- $\pi$ -A molecular system as a dye sensitizer in organic solar cell application has improve the solar conversion efficiency (Teo *et al.*, 2017).

### 1.3 The generation of solar cell application and materials

Solar cells are generally divided into three generations (Figure 1.5) depending on the time and classes of materials used for fabrication. The first (1<sup>st</sup>) generation of solar cells are commonly referred to the silicon-based solar cells which employed silicon wafer-based technology and dominate the photovoltaic market, owing to high efficiencies (Kibria *et al.*, 2014; Omar *et al.*, 2020). The second (2<sup>nd</sup>) generation known as thin film solar cells offer prospects for a significant reduction in material costs by eliminating the high-cost silicon wafer.

Third (3<sup>rd</sup>) generation solar cells are quite different from the former generation's as the traditional p-n junction is not required to separate photogenerated charge carrier. Taking into account the pros and cons of the former solar cells technologies, researchers have proposed the quantum dot-sensitized solar cells ( $\eta \approx 10\%$ ), organic solar cells ( $\eta \approx 11\%$ ), DSSCs ( $\eta \approx 13\%$ ) and currently emerging hybrid perovskite solar cells ( $\eta \approx 22\%$ ) as the third generation of solar cells (Ananthakumar *et al.*, 2019; Omar *et al.*, 2020). In the past few years, there have been a growing interest in developing DSSCs as low-cost alternatives solar cells to the conventional amorphous silicon solar cells due to the simplicity in its fabrication process under ambient conditions (Akila *et al.*, 2019).

	1G	2G	3G
Technology	Wafer-based (single junction, mono- or polycrystalline silicon)	Thin film (CdTe, CIGS, a-Si)	Organic (Polymer, Small molecule), DSSC
Advantages	High quality, low-defect, high efficiency	High material utilisation, lower cost	Non-toxic, abundant, low-cost, short payback, transparent
Challenges	High consumption of active material (Si)	Scarcity or toxicity of some materials	Optimizing lifetime-efficiency-cost trade-off

Figure 1.5 The first, second and third generation of solar cells (Organic Photovoltaics, n.d)

In general, a typical DSSC consists of three components, specifically dye-sensitized photoanode, counter electrode and redox electrolyte, which appears to be a sandwich-look like structure (Figure 1.6).

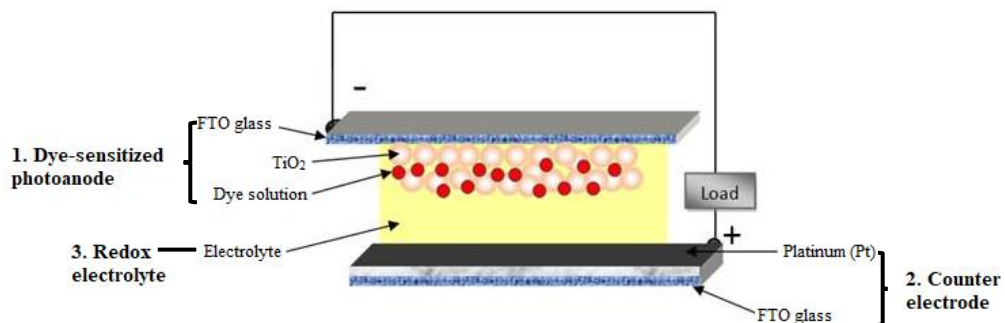


Figure 1.6 The structure of DSSC (Bakr *et al.*, 2016)

Dye sensitizer is the main material for the absorption and conversion efficiency in DSSC. The properties of the dye are tunable by matching different groups of  $\pi$ -donor and acceptor in the dyes' molecule (Wu *et al.*, 2010). An ideal dye sensitizer should possess some distinctive characteristics such as (1) having a strong absorption wavelength in visible range under light illumination; (2) comprising -H or =O groups which capable to anchor on the TiO<sub>2</sub> surface of semiconductor; (3) excellent stability in the ground, excited and oxidized states; and (4) having suitable redox potential

which will regenerate electrons immediately thru  $I^-/I_3^-$  in electrolyte (Ludin *et al.*, 2014; Shalini *et al.*, 2016; Lee *et al.*, 2017; Ung *et al.*, 2017). In this case, DSSC indicates a good alternative way in producing greener renewable energy with low production cost as compared to the inorganic semiconductor-based photovoltaic devices (Fahim *et al.*, 2018; Khan *et al.*, 2019).

Stability of DSSCs have been the key issue to manage since the organometallic dyes and liquid electrolytes are unstable for a long period (Ananthakumar *et al.*, 2019). External factors such as the humidity from atmosphere, degradation of all DSSC components by UV light irradiation from the sunlight especially for organic dyes and leaking of liquid electrolyte from the device are the main challenges faced in enhancing the stability of DSSC (Castro-Hermosa *et al.*, 2017; Ananthakumar *et al.*, 2019).

#### **1.4 Problem Statement**

Dye-sensitized solar cells (DSSCs) have been intensively investigated due to the potential for low cost and high optical absorption by organic materials (Lee *et al.*, 2017). Most of the reported metal-free chalcone derivatives have the low absorption coefficient in the visible region (Anandkumar *et al.*, 2017; Teo *et al.*, 2017; Makhlouf *et al.*, 2018). Therefore, there is a prevailing need to investigate the new metal organic material for photovoltaic conversion in order to achieve large absorption coefficient within the UV-Vis region.

Previously, the ruthenium complexes sensitizer (N719) has achieved the highest power conversion efficiencies which surpassing ~7% in DSSC application (Quang *et al.*, 2021; Althagafi & El-Metwaly, 2021). However, some limitations raised from the ruthenium dyes such as scarcity, toxicity and expensive issues caused significant progress in designing new organic materials with donor- $\pi$ -acceptor

architectures (Mori *et al.*, 2016). The key strategy in synthesizing donor- $\pi$ -acceptor organic structure is to allow the efficient energy transfers of electrons from the electron-donating group to electron-withdrawing group that anchored on the TiO<sub>2</sub> surface.

Recently, many researchers have started giving attention to the mono-based chalcone as well as the derivatives particularly in DSSC application. Most of the organic DSSC give a low efficiency which is less than 1% (Teo *et al.*, 2017). Meanwhile, the conversion efficiency of metal organic in DSSC also found to have nearly the same efficiency (5-6%) with the inorganic material (8-10%) (Alhorani *et al.*, 2020). In a report by Chauhan *et al.* (2016), ferrocene derivatives are treated as good photosensitive dyes in DSSCs for the photovoltaic performance. Furthermore, ferrocene substituted chalcones have also been reported with various application due to their well-defined redox potential (Erasmus 2011, Wu *et al.*, 2006). However, the use of ferrocenyl chalcone as sensitizer is less explored in term of DSSC application.

## 1.5 Objectives

1. To synthesis a new series of ferrocenyl chalcone derivatives featuring D- $\pi$ -A chalcones as dye sensitizer in organic photovoltaic cell.
2. To characterize the synthesized compound *via* several selected spectroscopic analyses in comparison with theoretical calculation using Density Functional Theory (DFT) method.
3. To investigate the effect of different substituent acceptor groups through structural-property relationships as potential photosensitizer material.
4. To evaluate the suitability of the studied ferrocenyl chalcone derivatives for potential dye-sensitized solar cells (DSSC) application.

## CHAPTER 2

### LITERATURE REVIEW

#### 2.1 Synthesis of Ferrocenyl Chalcone Derivatives

Chalcone derivatives structurally consist of two aryl groups which connected by  $\alpha, \beta$ -unsaturated ketone moiety (Zhang *et al.*, 2019). In recent times, a range of adapted methods and schemes for the synthesis of chalcone derivatives have been reported. Among the stated techniques, some researchers used Aldol condensation, Claisen-Schmidt condensation, Suzuki Coupling reaction, Wittig reaction, Friedel-Crafts acylation with cinnamoyl chloride or Photo-Fries rearrangement of phenyl cinnamates method in the preparation of chalcones (Nasir *et al.*, 2013). Even so, the Claisen-Schmidt condensation method is still in demand to be used as the synthesis method due to its simplicity and convenience with minimum side effects.

Based on the previous works, most of the reported ferrocenyl chalcones were prepared by the Claisen-Schmidt condensation method (Song *et al.*, 2006; Chauhan *et al.*, 2016; Trujillo *et al.*, 2017; Yadav *et al.*, 2019). The reaction involves cross aldol condensation of benzaldehyde and acetylferrocene in ethanol and the presence of potassium hydroxide (KOH) base as catalyst. The reaction mixture is neutralized with diluted hydrochloric acid (HCl) and crystallized using various solvent system to obtain the corresponding ferrocenyl chalcone. The synthetic scheme for one of the reported compounds is shown in Figure 2.1.

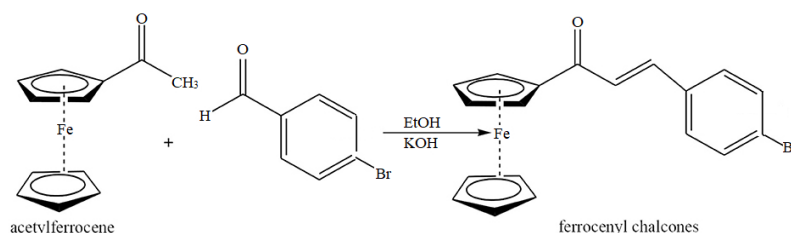


Figure 2.1 Synthesis scheme of (2E)-1-Ferrocenyl-3-phenyl-prop-2-en-1-one (Yadav *et al.*, 2019).

Chauhan *et al.* (2016) synthesized the ferrocenyl chalcones by base-catalyzed Claisen-Schmidt condensation between ferrocenecarbaldehyde and acetophenone in dry ethanol and an aqueous solution of KOH as catalyst under nitrogen atmosphere. The reaction mixture was then neutralized with diluted HCl and treated with column chromatography. The resultant reported product was reported in deep red colour precipitate.

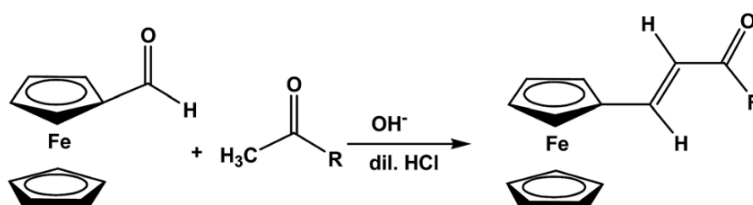


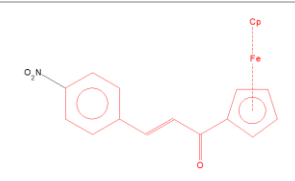
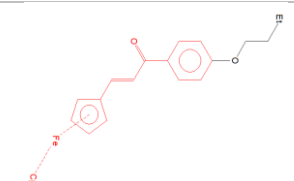
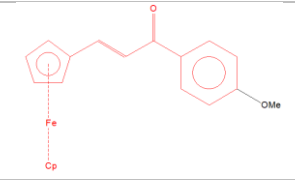
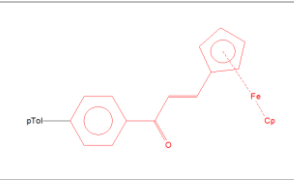
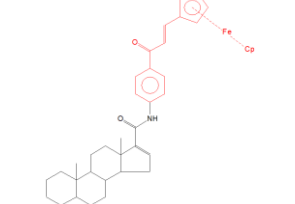
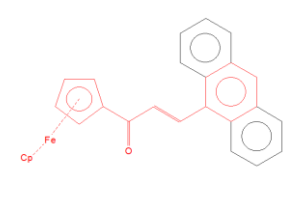
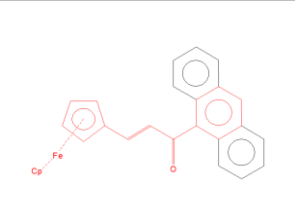
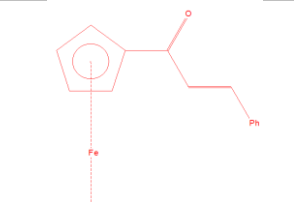
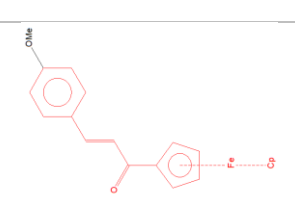
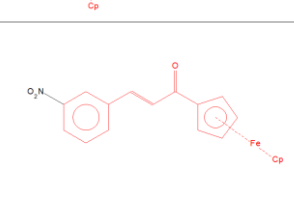
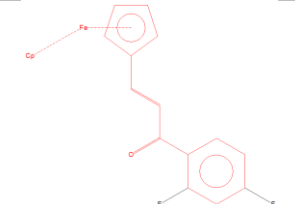
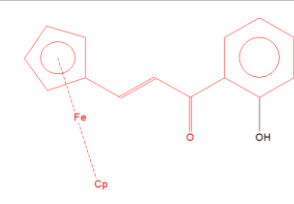
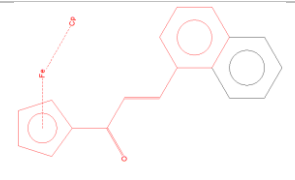
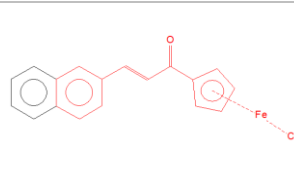
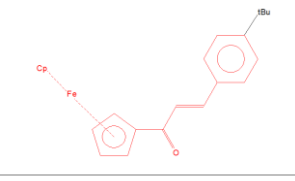
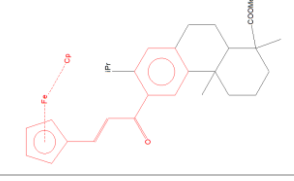

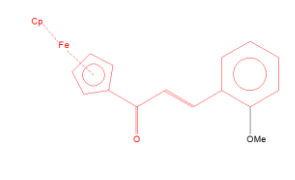
Figure 2.2 Synthesis scheme of ferrocenyl chalcone (Chauhan *et al.*, 2016).

Based on a search of the Cambridge Structural Database (Version 5.41, last update March 2020; Groom *et al.*, 2016), 29 single crystals of ferrocenyl chalcones were reported by previous studies in the past two decades. Table 2.1 shows the statistics of reported ferrocenyl chalcones which included CCDC numbers and the respective chemical structures.

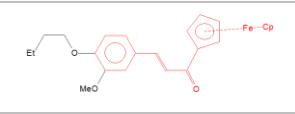
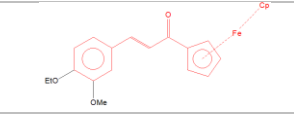
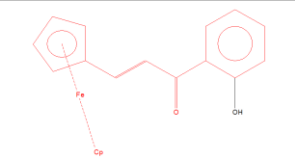
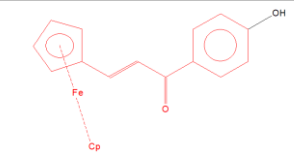
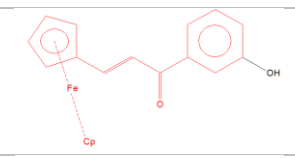
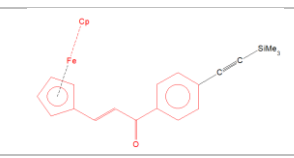
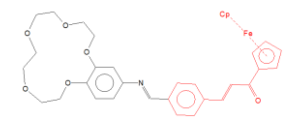
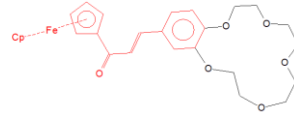
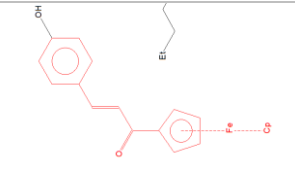
Table 2.1 List of the reported single crystals of ferrocenyl chalcones from previous studies.

Year	CCDC Number	Chemical Structure	Year	CCDC Number	Chemical Structure
2003	217895		2005	245554	

**Table 2.2** *Con't*

2006	257043		2006	257044	
2006	257154		2006	608337	
2007	619190		2008	661664	
2008	661665		2008	700338	
2008	702402		2008	705939	
2010	763129		2010	786471	
2012	823245		2012	836352	
2012	839534		2012	913017	
2013	935420		2014	987910	

**Table 2.3** *Con't*

2016	1407296		2016	1407297	
2016	1480595		2016	1480596	
2016	1480597		2016	1470200	
2017	1485208		2017	1485209	
2017	1501138				

## 2.2 Fourier Transform Infrared (FTIR) Vibrational Studies

Fourier Transform Infrared Analysis (FTIR) is an analytical technique specifically for identifying the existence of functional groups in the molecule (Muller *et al.*, 2009). The classical potassium bromide (KBr) pellet method requires sample preparation by pressing powder into a pellet and the spectral range of infrared region observed in the wave number ranging from 400-4000  $\text{cm}^{-1}$ . On the other hand, Bukowski and Monti (2007) reported that Attenuated Total Reflection-Fourier Transform Infrared (ATR-FTIR) Spectroscopy provides quantitative analysis of samples without requiring complex preparations. The absorbance spectra of ATR-FTIR are recorded in the region of 600-4000  $\text{cm}^{-1}$ . The focus studies for ferrocenyl chalcones primarily on the C-H stretching, C=O and C=C stretching of enone bridge, C=C stretching of ferrocene ring and Fe-ring (Fe-Cp) stretching. Some reported values of the vibrational frequency FTIR for ferrocenyl chalcones are tabulated in Table 2.2.



Table 2.2 Assignment of some characteristic vibrational frequencies of ferrocenyl chalcone.

Stretching ( $\nu$ ) vibrational mode	Experimental ( $\text{cm}^{-1}$ )	Literature
$\nu\text{C-H}$	3083 3086-3105 3050-3100	(Twinkle <i>et al.</i> , 2020) (Trujillo <i>et al.</i> , 2017) (Chauhan <i>et al.</i> , 2016)
$\nu\text{C=O}$	1654 1628-1630 1639-1654 1646-1653 1630-1694 1643-1662 1646-1653	(Twinkle <i>et al.</i> , 2020) (Trujillo <i>et al.</i> , 2017) (Yadav <i>et al.</i> , 2019) (Muller <i>et al.</i> , 2012) (Chauhan <i>et al.</i> , 2016) (Attar <i>et al.</i> , 2011) (Elizabeth Erasmus, 2018)
$\nu\text{C=C}$ (alkene)	1588 1569 1562-1597 1557-1595 1581-1608	(Twinkle <i>et al.</i> , 2020) (Trujillo <i>et al.</i> , 2017) (Yadav <i>et al.</i> , 2019) (Chauhan <i>et al.</i> , 2016) (Attar <i>et al.</i> , 2011)
$\nu\text{C=C}$ (Cp)	1330-1377 1207-1364 1088-1271	(Delgado-Rivera <i>et al.</i> , 2017) (Chauhan <i>et al.</i> , 2016)
$\nu\text{Fe-Cp}$	481-483 483-500 485	(Liu <i>et al.</i> , 2018) (Chauhan <i>et al.</i> , 2016)

Cp: cyclopentadienyl ring of ferrocene.

Based on the reported studies, most of the aliphatic C-H stretching vibrations are found to be weak in the region of 3000-3050  $\text{cm}^{-1}$  for the vinyl group due to the charge transfer from the hydrogen atom to carbon atom (Maidur *et al.*, 2018). Generally, these vibrations are in the expected region for chalcones indicating that the C-H vibrations are not influenced by any substituent (Kumar *et al.*, 2017).

As previously reported by Twinkle *et al.* (2020), the vibrations of  $\alpha,\beta$ -unsaturated carbonyl group ( $\nu\text{C=C}$ ) are highly sensitive to the degree of charge transfer between donor and acceptor groups. The attachment of electron-donor ferrocene moiety and electron-acceptor pyrimidine moiety through the  $\pi$ -conjugated system induces the lowering of the C=C stretching mode (1588  $\text{cm}^{-1}$ ) and proved that ICT occurred within the structure (Twinkle *et al.*, 2020).

The wavenumber of the C=O stretching vibrations for the enones depends mainly on the binding force that involve the inductive (Panicker *et al.*, 2015), conjugative (Kumar *et al.*, 2017), steric effects (Zainuri *et al.*, 2018) and lone pair of electron on oxygen atom (Naik *et al.*, 2020). Furthermore, the presence of strong electronegative substituent also plays a role in shifting the vibrational frequency of C=O mode from the normal position which result in higher wavenumber (Rawat *et al.*, 2021).

No significant change was observed in the stretching bands for Fe-Cp which proved that ferrocene ring of ligand remained intactly upon complexation (Liu *et al.*, 2018). The spectrum of ferrocenyl chalcone bearing a methyl pyrimidine (Twinkle *et al.*, 2020) is shown in Figure 2.3.

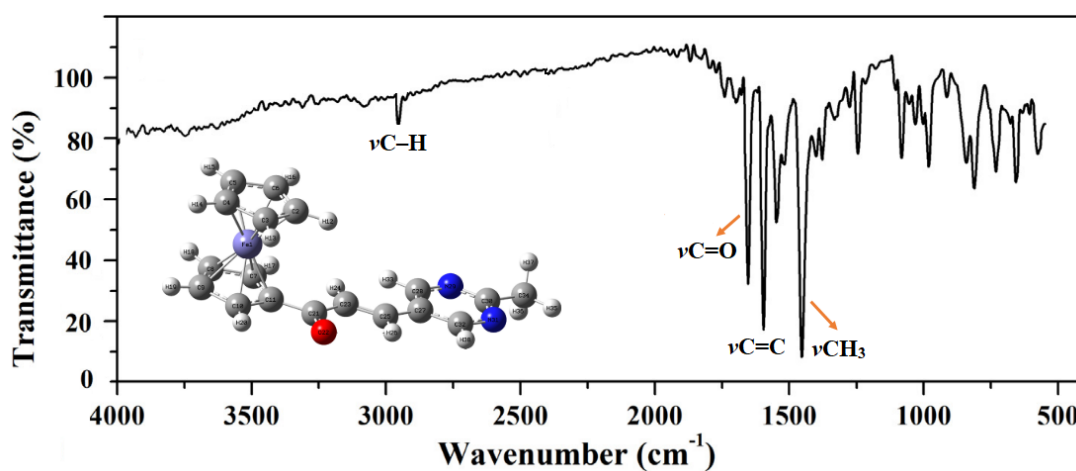


Figure 2.3 FTIR spectrum of methyl pyrimidine substituted ferrocenyl chalcone (Twinkle *et al.*, 2020).

According to Colthup and co-workers (1990), a significant difference can be noted between compounds in which the C=O and C=C have *trans* or *cis* orientation. In *s-cis*, the C=O (1687-1700  $\text{cm}^{-1}$ ) and C=C (1617-1624  $\text{cm}^{-1}$ ) bands are further apart as compared to *s-trans*; C=O (1675-1690  $\text{cm}^{-1}$ ) and C=C (1617-1644  $\text{cm}^{-1}$ ).

### 2.3 Nuclear Magnetic Resonance (NMR) Studies

The synthesized chalcones can be characterized by two types of NMR spectroscopy which are  $^1\text{H}$  and  $^{13}\text{C}$  NMR. The studies for  $^1\text{H}$  NMR of ferrocenyl chalcones primarily focus on the enone bridge and ferrocene derivative (Figure 2.4). There are a few studies reported on the NMR analyses for the ferrocenyl chalcones as tabulated in Table 2.3 and Table 2.4 for  $^1\text{H}$  and  $^{13}\text{C}$  NMR, respectively.

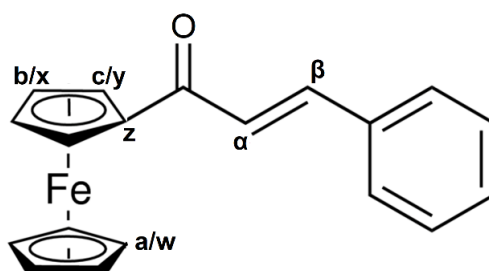


Figure 2.4 The assignment of  $^1\text{H}$  NMR of ferrocenyl chalcone.

Table 2.3  $^1\text{H}$  isotropic chemical shifts (ppm)

Literature	$^1\text{H}$ NMR				
	H $\alpha$	H $\beta$	Cp1	Cp2	
			Ha	Hb	Hc
(Muller <i>et al.</i> , 2012)	7.09-7.19	7.76-7.87	4.23-4.28	4.60-4.66	4.93-4.98
(D. K. Yadav <i>et al.</i> , 2019)	7.16-7.21	7.60-7.63	4.19-4.24	4.57-4.66	4.90-4.94
(Khan <i>et al.</i> , 2017)	7.01-7.12	7.75-8.06	4.22-4.24	4.60-4.65	4.90-4.95

Cp1: unsubstituted; Cp2: substituted cyclopentadiene ferrocene rings.

The ethylenic protons of enone moiety (H $\alpha$  and H $\beta$ ) exhibit two doublets at the range of 7.01-7.21 and 7.60-8.06 ppm as tabulated in Table 2.3. Furthermore, the typical pattern for  $^1\text{H}$  NMR of ferrocenyl chalcones show three cyclopentadienyl proton signals at  $\pm 4.2$ ,  $\pm 4.6$  and  $\pm 4.9$  ppm with the proton integral area ratio of 5:2:2. The singlet appearing at  $\pm 4.2$  ppm, assigned as H $\alpha$  (Figure 2.4) arises from excitation of five equivalent aromatic protons on the unsubstituted cyclopentadienyl ring (Cp1).

Whereas the other two singlets at  $\pm 4.6$  and  $\pm 4.9$  ppm, appointed as **Hb** and **Hc**, respectively are associated to the substituted cyclopentadienyl ring (Cp2), integrating for two protons each. According to Muller *et al.* (2012), the  $^1\text{H}$  chemical shifts of the ferrocene derivative would not vary substantially when modifying the substituent group on the other end of ferrocenyl chalcone (Figure 2.5a).

Based on the Table 2.3, the electronegative C=O functional group polarizes the electron distribution and appears at the lowest field values (191.17-193.64 ppm). Furthermore, 10 carbon-ferrocene signals of ferrocenyl chalcones appeared as four peaks (Cw, Cx, Cy and Cz) in the range of 68.24-81.07 ppm. Generally, an intense carbon peak (Cw) for the Cp1 can be observed due to the overlapping of five equivalent aromatic carbons as shown in Figure 2.5b (Khan *et al.*, 2019).

Table 2.4  $^{13}\text{C}$  isotropic chemical shifts (ppm)

Literature	$^{13}\text{C}$ NMR				
	C=O	C $\alpha$	C $\beta$	Cp1	Cp2
				Cw	Cx, Cy, Cz
(D. K. Yadav <i>et al.</i> , 2019)	191.17-192.92	117.80-126.51	137.14-141.24	69.12-70.00	68.24-69.95 72.48-73.23 79.83-81.05
(Khan <i>et al.</i> , 2017)	192.74-193.64	114.39-123.37	139.43-149.22	70.06-70.14	69.60-69.88 72.50-72.92 80.46-81.07

Cp1: unsubstituted; Cp2: substituted cyclopentadiene ferrocene rings.

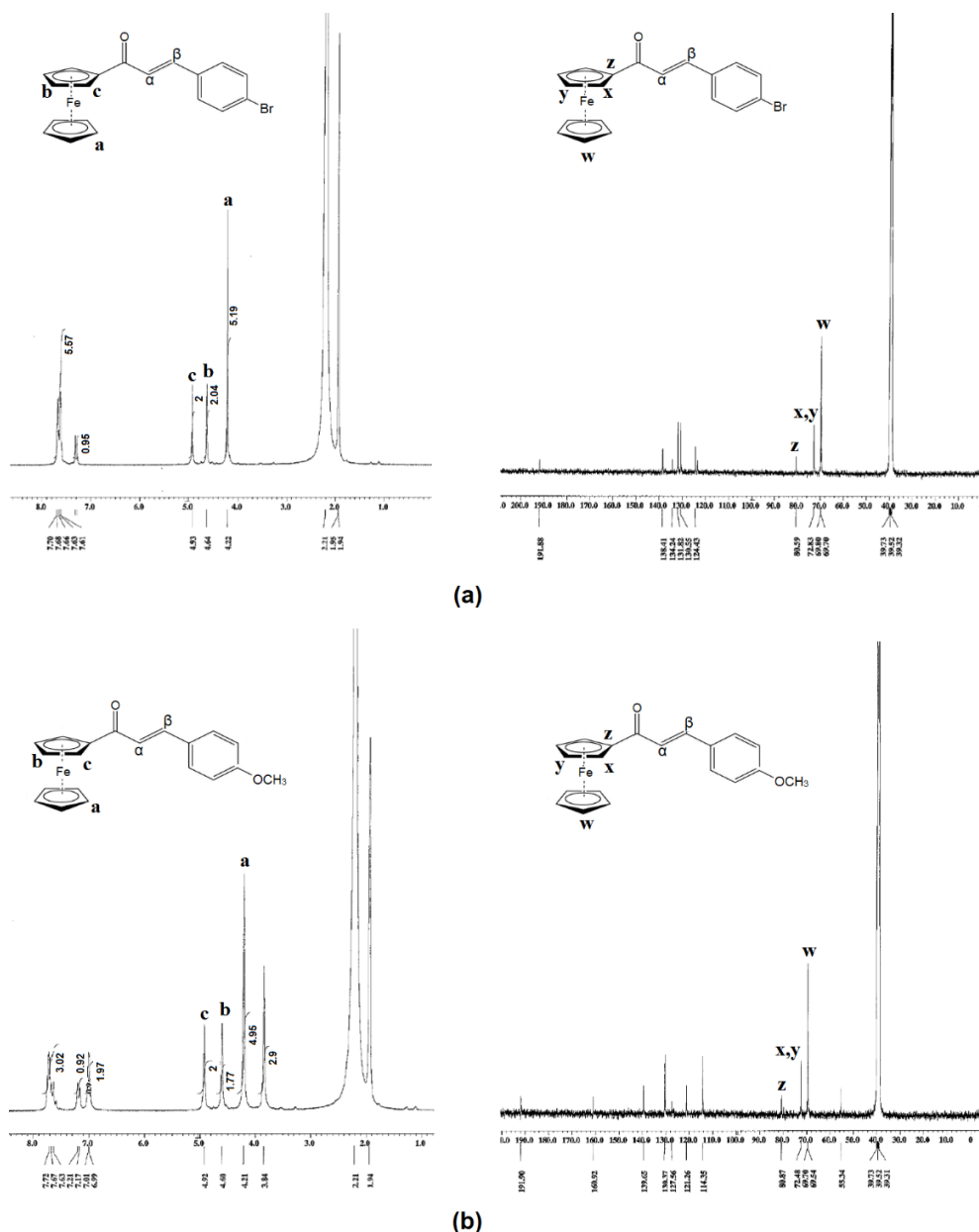


Figure 2.5 The spectrum of (a) <sup>1</sup>H NMR and (b) <sup>13</sup>C NMR (Yadav *et al.*, 2019).

## 2.4 UV-Visible Spectroscopic Studies

The conductivity of material is determined by the energy band gap. This band gap is located between valence and conduction bands (Sang-aroon *et al.*, 2019). The energy difference between the two bands will give the minimum energy required for an electron to break free of its bound state (Tripathi *et al.*, 2020). Figure 2.6 shows the absorption spectrum of (*E*)-chalcone that having an absorption maximum wavelength ( $\lambda_{\text{max}}$ ) at 310 nm (Jumina *et al.*, 2019).

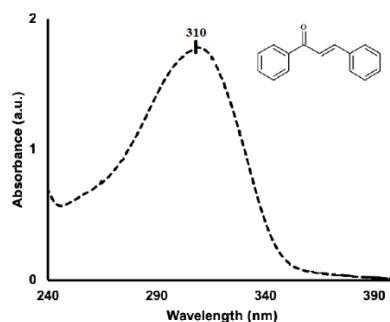


Figure 2.6 Absorption spectrum of (*E*)-chalcone (Jumina *et al.*, 2019).

Ferrocenyl chalcone that arise from the modification of the chalcone by substituting the end capped with ferrocene derivative has expanded the  $\lambda_{\max}$  of the compound. The metal-to-ligand charge transfer (MLCT) characters in ferrocene derivative pushed more electrons into the molecule, resulting larger  $\lambda_{\max}$  (Paul *et al.*, 2019). Table 2.5 shows the maximum absorbance peak and energy band gap of some reported studies for ferrocenyl chalcones.

Table 2.5 The  $\lambda_{\max}$  (in nm) and energy band gap (in eV) of ferrocenyl chalcones from previous studies

Literature	Maximum absorption, $\lambda_{\max}$ (nm)	Energy gap (eV)
(Muller <i>et al.</i> , 2012)	490	2.45
(Hernández-Ortiz <i>et al.</i> , 2020)	438, 440, 442	2.30, 2.37, 2.58
(Trujillo <i>et al.</i> , 2017)	498	2.03
(Chauhan <i>et al.</i> , 2016)	510	2.43

Maynadié *et al.* (2006) has reported UV light absorption spectra in acetonitrile of ferrocenyl chalcone  $[(C_5H_5)Fe(C_5H_4COCH=CHC_6H_4NEt_2)]$ ; **A**] and the common feature of organic derivative  $(CH_3COCH=CHC_6H_4NEt_2)$ ; **B**] as illustrated in Figure 2.7. From the figure, it revealed that **A** and **B** spectra have almost similar pattern of absorption bands. The absorption spectrum of **A** shows two characteristic bands (254 and 404 nm) with an extended long-wavelength absorption tail. In **B**, aside from the

first band (250 nm), it also showed an intense band forming around 385 nm. Based on this research, 250 and 254 nm bands were assigned to the  $\pi \rightarrow \pi^*$  transition characteristic of aromatic ketones, whereas the weak shoulder band (~330 nm) observed only in **A** was due to the  $n \rightarrow \pi^*$  transition. Apart from that, the intense long-wavelength band (404 nm) was attributed to charge transfer (CT) between the donor amino group and the acceptor carbonyl group. This CT band in **A** was slightly red-shifted with respect to that **B**, owing to its larger conjugated system. Bai (2019) stated that as the conjugated system become larger, the absorption band wavelength tends to shift towards longer wavelength region and the absorption band become larger. In this case, the maximum absorption band for both compounds were appeared identical. However, a broad low-intensity band can be observed only in **A** which located above 480 nm that has been assigned to d-d transition of iron in ferrocene. Hence, the broad absorption spectrum observed in **A** usually showing that the compound has acceptable sunlight harvesting capability for solar application (Maynadié *et al.*, 2006; Hernández-Ortiz *et al.*, 2020).

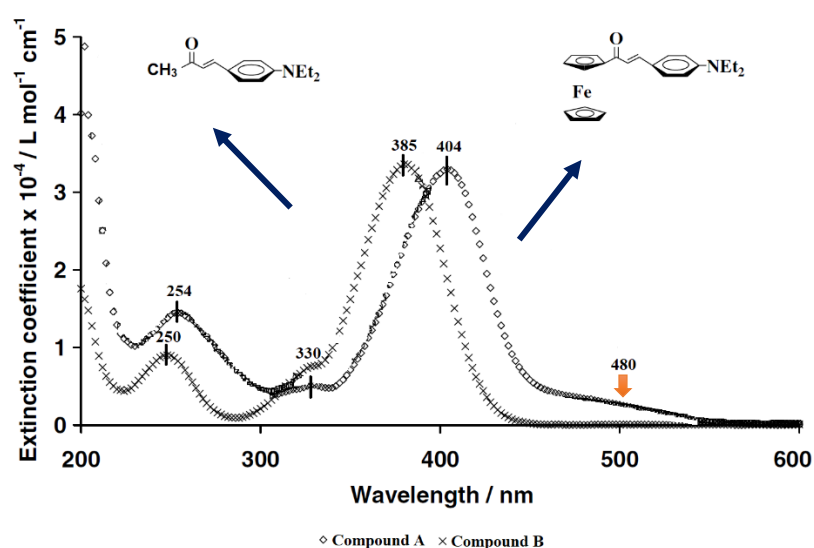


Figure 2.7 Absorption spectra of compounds (Maynadié *et al.*, 2006).

Trujillo *et al.* (2017) studied the effect of five different solvents which were diethyl ether, dichloromethane (DCM), acetone, acetonitrile (MeCN), and dimethyl sulfoxide (DMSO) on the UV-Vis absorption spectra (Figure 2.8). The wavelength shifts corresponding to the  $\lambda_{\max}$  were tabulated in Table 2.6. The absorption spectra of the compound showed two characteristic bands for all different solvents. The first band in the region of ultraviolet, which is between 262–356 nm. This band represented  $\pi \rightarrow \pi^*$  transition in the compound. The second band which lied in visible region was observed between 423–513 nm in less intense peak. This band was assigned for the  $d \rightarrow \pi^*$  of MLCT transition from the iron Fe (d) orbital to the organic moiety orbital ( $\pi^*$ ). Based on the result, the absorption spectra were observed to shift into higher maximum wavelength with increases in the solvent polarity (diethyl ether < DCM < acetone < MeCN < DMSO). Solvent polarity caused red shifted of maximum absorption due to attractive polarization forces between solvent (Anizaim *et al.*, 2019) and absorber associated to a decrease in ground and excited states energy (Zainuri *et al.*, 2018).

Table 2.6 UV-Vis absorption maximum of the compound in different solvents (Trujillo *et al.*, 2017).

Solvent	Diethyl ether	DCM	Acetone	MeCN	DMSO
Absorption band ( $\lambda$ )	498 nm 345 nm	513 nm 350 nm 327 nm	423 nm 262 nm	510 nm 350 nm	502 nm 356 nm



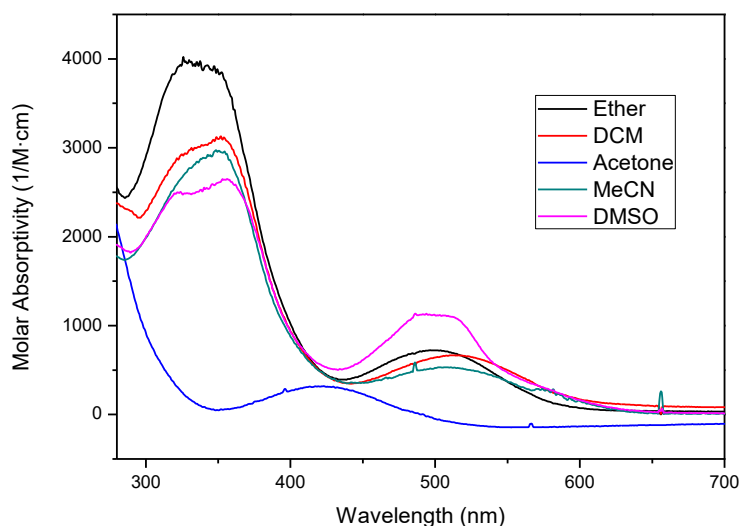


Figure 2.8 The experimental absorption spectra of  $1.1 \times 10^{-4}$  mM (*E*)-3-Ferrocenyl-1-(2-hydroxy-4-methoxyphenyl)-prop-2-en-1-one in different solvents (Trujillo *et al.*, 2017).

Muller *et al.* (2012) also reported UV-Vis spectra of seven ferrocenyl chalcones with different substituents on the *para*-position of the phenyl group ( $\text{Fc-CO-CH=CH-C}_6\text{H}_4\text{R}$ , where R = OCH<sub>3</sub>, CH<sub>3</sub>, Ph, <sup>t</sup>Bu, H, Br and CF<sub>3</sub>) as shown in Figure 2.9. The UV-Vis spectra of these ferrocenyl chalcones showed two characteristic peaks around 380 and 490 nm with an absorption tail that extended till  $\pm 710$  nm. The first peak at  $\pm 380$  nm for the compounds appeared more as shoulder rather than well-defined peak which assigned for  $\pi\text{-}\pi^*$  transition of the  $\alpha,\beta$ -unsaturated carbonyl conjugation with the ferrocenyl moiety. Likewise, the second broad peak at  $\pm 490$  nm was attributed to the d-d transition of the Fe in the ferrocene derivative, also referred to MLCT. The alteration of the substituent R-group to the phenyl ring in ferrocenyl chalcones led to a change in the electronic communication of the compounds (Erasmus, 2017). The polarity of the ferrocenyl chalcones have been influenced by the electron-donating and -withdrawing effects of the R-groups (Nair *et al.*, 2018). As the electron withdrawing properties of the R-groups increases, hence the compound turned to be more polarized and the absorption maximum ( $\lambda_{\text{max}}$ ) at  $\pm 490$

nm will be subjected to bathochromic shift (red shift) towards higher wavelength (Sun *et al.*, 2019) as shown in Table 2.7.

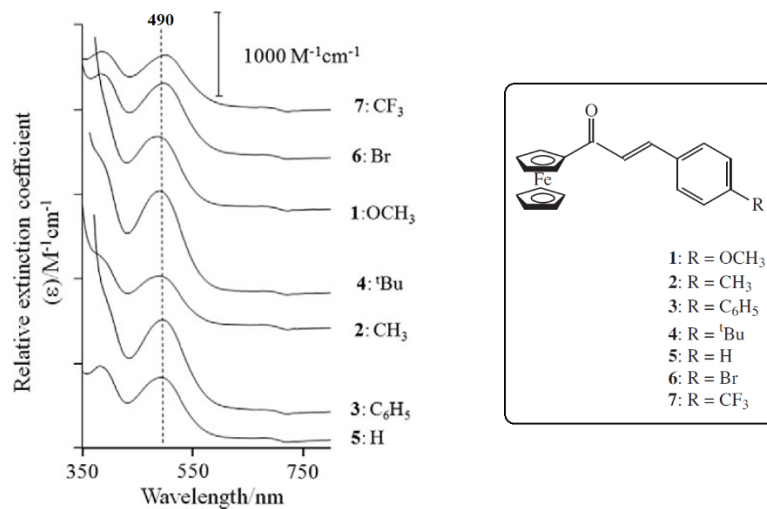


Figure 2.9 UV-Vis spectra of 7 ferrocenyl chalcones in acetonitrile (Muller *et al.*, 2012).

Table 2.7 Some characterization of different R-groups substituents in ferrocenyl chalcones

Compound	R-group substituent	$\lambda_{\max}$ (nm)
<b>1</b>	OCH <sub>3</sub>	487
<b>2</b>	CH <sub>3</sub>	487
<b>3</b>	Ph	495
<b>4</b>	<sup>t</sup> Bu	491
<b>5</b>	H	491
<b>6</b>	Br	497
<b>7</b>	CF <sub>3</sub>	501

## 2.5 X-ray Diffraction Studies

### 2.5.1 *Cis, trans, s-cis* and *s-trans* configurations

The flexible molecules of chalcones may exist in various conformations which include the *cis*, *trans*, *s-cis* and *s-trans* configurations (Figure 2.10). The *cis* or *trans* configurations of chalcone are presented by the hydrogen atoms of the double bond  $C_{\alpha}=C_{\beta}$ , while the *s-cis* or *s-trans* conformations are depending on the  $C=O$  with respect to the vinylenic double bond ( $C_{\alpha}=C_{\beta}$ ) due to free rotation along the single bond between  $C=O$  and  $C_{\alpha}$  (Evrans Aksöz & Ertan, 2011). Among all designed configurations, the *s-cis* conformation has been identified as the most stable conformer and appeared to be almost planar (Evrans Aksöz & Ertan, 2011).

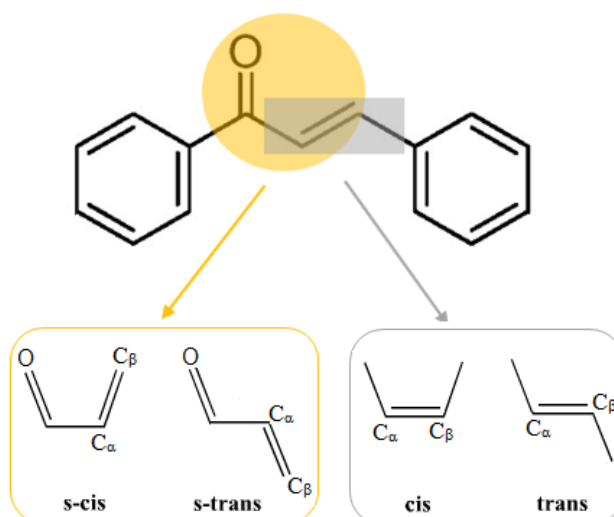


Figure 2.10 Different type of configurations in chalcone.

Jung *et al.* (2008) reported two ferrocenyl chalcones containing the anthracenyl group, in which Fc and Anth are the notation for ferrocene and anthracene derivatives, respectively. Based on Figure 2.11, the enone linkages possess different conformations for Fc-Anth (*s-cis*) and Anth-Fc (*s-trans*). In both compounds, the substituted Cp rings have been proven to be almost co-planar with enone linkages. However, the significant deviation raised from the planar anthracenyl groups and the enone linkages caused the

different in structure conformations within both compounds (Jung *et al.*, 2008; Zainuri *et al.*, 2018). Therefore, it may be concluded that the substituted groups are responsible or liable for the *s-cis* and *s-trans* conformations.

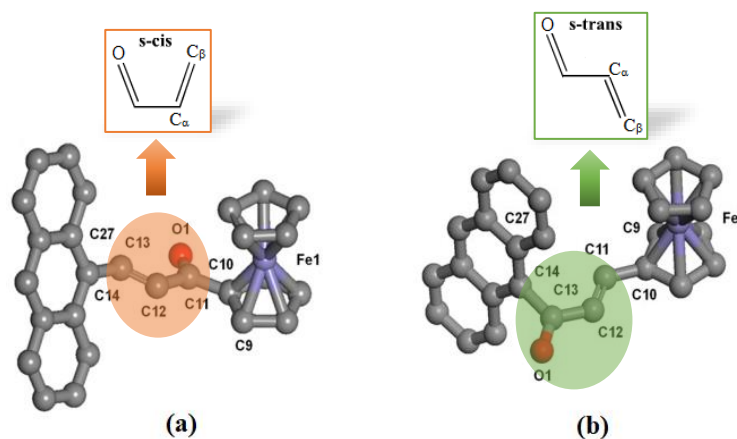


Figure 2.11 Molecular structures of (a) Fc-Anth and (b) Anth-Fc (Jung *et al.*, 2008).

Likewise, Attar *et al.* (2011) reported the *s-cis* conformation of (2*E*)-1-(2,4-difluorophenyl)-3-ferrocenyl-2-propen-1-one and (2*E*)-1-(2-furanyl)-3-ferrocenyl-2-propen-1-one (Figure 2.12) showing a slightly planar configuration between Cp2 ring of ferrocene derivative and also enone bridge.

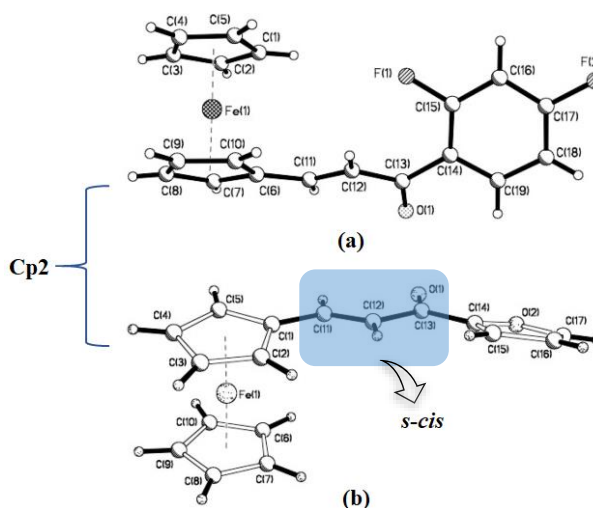


Figure 2.12 Molecular structure of (a) (2*E*)-1-(2,4-difluorophenyl)-3-ferrocenyl-2-propen-1-one and (b) (2*E*)-1-(2-furanyl)-3-ferrocenyl-2-propen-1-one (Attar *et al.*, 2011).

## 2.5.2 Crystal packing

The understanding of molecular structures and crystal packing are important in analysing intramolecular charge transfer (ICT) of the compound. In the previously reported structure of halogenated chalcone as shown in Figure 2.13a, the ICT associated with an electron cloud movement through a  $\pi$ -conjugated framework. The existence of intermolecular C—H $\cdots$ O hydrogen bond interactions in the compound play pivotal roles for the crystal packing pattern (Kwong *et al.*, 2018) and in generating the photo-induced electrons to be injected into the conduction band of the TiO<sub>2</sub> semiconductor (Lee *et al.*, 2017). The crystal packing showed that the molecules are joined into an infinite zig-zag chain *via* C—H $\cdots$ O interaction with side-by-side arrangement that leads to a faster charge transfer (Figure 2.13b).

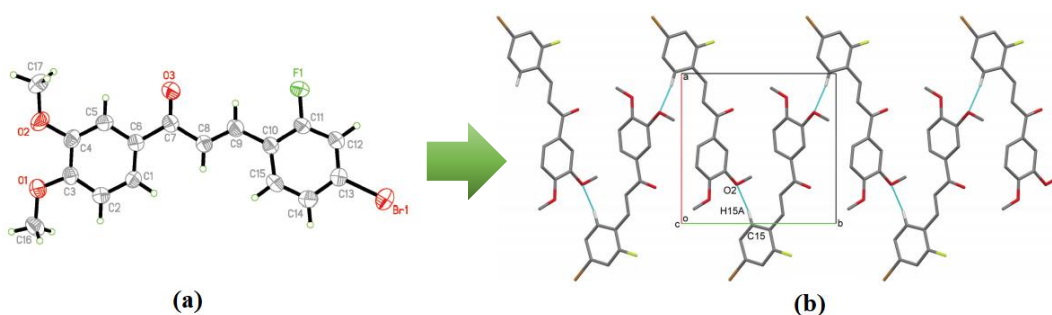


Figure 2.13 (a) The ORTEP diagram; (b) The crystal packing of (*E*)-3-(4-bromophenyl)-1-(3,4-dimethoxyphenyl)prop-2-en-1-one (Kwong *et al.*, 2018).

Reporting the molecular packing of 1-(4-methoxyphenyl)-3-(4-*N,N*-dimethyl amino phenyl)-2-propen-1-one as shown in Figure 2.14a, Zhao *et al.* (2021) observed that the molecules are stacked up in layered structures *via* C—H $\cdots$ O interaction which further connected into head-to-head fashion (Figure 2.14b). This ensures the electronic delocalization within the molecule which helps to possess charge injection for solar application.